

Imaging skeletal muscle using second harmonic generation and coherent anti-Stokes Raman scattering microscopy

Christian P. Pfeffer,¹ Bjorn R. Olsen,¹ Feruz Ganikhanov,² and François Légaré^{3,*}

¹Harvard School of Dental Medicine, 188 Longwood Avenue, Boston, MA 02115, USA

²Department of Physics, PO BOX 6315, West Virginia University, Morgantown, WV 2650, USA

³Institut National de la Recherche Scientifique, Centre Énergie Matériaux et Télécommunications, 1650 Boulevard Lionel-Boulet, Varennes, Qc Canada J3X1S2

*legare@emt.inrs.ca

Abstract: We describe experimental results on label free imaging of striated skeletal muscle using second harmonic generation (SHG) and coherent anti-Stokes Raman scattering (CARS) microscopy. The complementarity of the SHG and CARS data makes it possible to clearly identify the main sarcomere sub-structures such as actin, myosin, acto-myosin, and the intact T-tubular system as it emanates from the sarcolemma. Owing to sub-micron spatial resolution and the high sensitivity of the CARS microscopy technique we were able to resolve individual myofibrils. In addition, key organelles such as mitochondria, cell nuclei and their structural constituents were observed revealing the entire structure of the muscle functional units. There is a noticeable difference in the CARS response of the muscle structure within actin, myosin and t-tubule areas with respect to laser polarization. We attribute this to a preferential alignment of the probed molecular bonds along certain directions. The combined CARS and SHG microscopy approach yields more extensive and complementary information and has a potential to become an indispensable method for live skeletal muscle characterization.

©2011 Optical Society of America

OCIS codes: (180.4315) Nonlinear microscopy; (190.4160) Multiharmonic generation.

References and links

1. T. P. Burghardt, K. Ajtai, D. K. Chan, M. F. Halstead, J. Li, and Y. Zheng, "GFP-tagged regulatory light chain monitors single myosin lever-arm orientation in a muscle fiber," *Biophys. J.* **93**(6), 2226–2239 (2007).
2. M. E. Quinlan, J. N. Forkey, and Y. E. Goldman, "Orientation of the myosin light chain region by single molecule total internal reflection fluorescence polarization microscopy," *Biophys. J.* **89**(2), 1132–1142 (2005).
3. E. Savio-Galimberti, J. Frank, M. Inoue, J. I. Goldhaber, M. B. Cannell, J. H. Bridge, and F. B. Sachse, "Novel features of the rabbit transverse tubular system revealed by quantitative analysis of three-dimensional reconstructions from confocal images," *Biophys. J.* **95**(4), 2053–2062 (2008).
4. R. M. Murphy, J. P. Mollica, and G. D. Lamb, "Plasma membrane removal in rat skeletal muscle fibers reveals caveolin-3 hot-spots at the necks of transverse tubules," *Exp. Cell Res.* **315**(6), 1015–1028 (2009).
5. F. Helmchen and W. Denk, "Deep tissue two-photon microscopy," *Nat. Methods* **2**(12), 932–940 (2005).
6. C. B. Schaffer, B. Friedman, N. Nishimura, L. F. Schroeder, P. S. Tsai, F. F. Ebner, P. D. Lyden, and D. Kleinfeld, "Two-photon imaging of cortical surface microvessels reveals a robust redistribution in blood flow after vascular occlusion," *PLoS Biol.* **4**(2), e22 (2006).
7. P. J. Campagnola and L. M. Loew, "Second-harmonic imaging microscopy for visualizing biomolecular arrays in cells, tissues and organisms," *Nat. Biotechnol.* **21**(11), 1356–1360 (2003).
8. R. M. Williams, W. R. Zipfel, and W. W. Webb, "Interpreting second-harmonic generation images of collagen I fibrils," *Biophys. J.* **88**(2), 1377–1386 (2005).
9. D. Oron, D. Yelin, E. Tal, S. Raz, R. Fachima, and Y. Silberberg, "Depth-resolved structural imaging by third-harmonic generation microscopy," *J. Struct. Biol.* **147**(1), 3–11 (2004).
10. D. Débarre, W. Supatto, A. M. Pena, A. M. Fabre, T. Tordjmann, L. Combettes, M. C. Schanne-Klein, and E. Beaurepaire, "Imaging lipid bodies in cells and tissues using third-harmonic generation microscopy," *Nat. Methods* **3**(1), 47–53 (2006).

11. C. L. Evans, E. O. Potma, M. Puoris'haag, D. Côté, C. P. Lin, and X. S. Xie, "Chemical imaging of tissue in vivo with video-rate coherent anti-Stokes Raman scattering microscopy," *Proc. Natl. Acad. Sci. U.S.A.* **102**(46), 16807–16812 (2005).
12. H. Wang, Y. Fu, P. Zickmund, R. Shi, and J. X. Cheng, "Coherent anti-stokes Raman scattering imaging of axonal myelin in live spinal tissues," *Biophys. J.* **89**(1), 581–591 (2005).
13. C. P. Pfeiffer, B. R. Olsen, F. Ganikhanov, and F. Légaré, "Multimodal nonlinear optical imaging of collagen arrays," *J. Struct. Biol.* **164**(1), 140–145 (2008).
14. U. Resch-Genger, M. Grabolle, S. Cavaliere-Jaricot, R. Nitschke, and T. Nann, "Quantum dots versus organic dyes as fluorescent labels," *Nat. Methods* **5**(9), 763–775 (2008).
15. A. Shiohara, A. Hoshino, K. Hanaki, K. Suzuki, and K. Yamamoto, "On the cyto-toxicity caused by quantum dots," *Microbiol. Immunol.* **48**(9), 669–675 (2004).
16. S. M. Burrows, R. D. Reif, and D. Pappas, "Investigation of photobleaching and saturation of single molecules by fluorophore recrossing events," *Anal. Chim. Acta* **598**(1), 135–142 (2007).
17. J.H. Kim, W.H. Kong, H.J. Kim, S.W. Sco, "Limitation of Q Dot as an In Vivo Cell Tracer," *Tissue Engineering and regenerative medicine* **6**, 307–312 (2009).
18. A. C. Kwan, D. A. Dombeck, and W. W. Webb, "Polarized microtubule arrays in apical dendrites and axons," *Proc. Natl. Acad. Sci. U.S.A.* **105**(32), 11370–11375 (2008).
19. S. V. Plotnikov, A. C. Millard, P. J. Campagnola, and W. A. Mohler, "Characterization of the myosin-based source for second-harmonic generation from muscle sarcomeres," *Biophys. J.* **90**(2), 693–703 (2006).
20. M. D. Duncan, J. Reintjes, and T. J. Manuccia, "Scanning coherent anti-Stokes Raman microscope," *Opt. Lett.* **7**(8), 350–352 (1982).
21. A. Zumbusch, G. R. Holtom, and X. S. Xie, "Three-dimensional vibrational imaging by coherent anti-Stokes Raman scattering," *Phys. Rev. Lett.* **82**(20), 4142–4145 (1999).
22. T. Hellerer, C. Axäng, C. Brackmann, P. Hillertz, M. Pilon, and A. Enejder, "Monitoring of lipid storage in *Caenorhabditis elegans* using coherent anti-Stokes Raman scattering (CARS) microscopy," *Proc. Natl. Acad. Sci. U.S.A.* **104**(37), 14658–14663 (2007).
23. E. Ralston, B. Swaim, M. Czapiga, W.-L. Hwu, Y.-H. Chien, M. G. Pittis, B. Bembi, O. Schwartz, P. Plotz, and N. Raben, "Detection and imaging of non-contractile inclusions and sarcomeric anomalies in skeletal muscle by second harmonic generation combined with two-photon excited fluorescence," *J. Struct. Biol.* **162**(3), 500–508 (2008).
24. S.-W. Chu, S.-Y. Chen, G.-W. Chern, T.-H. Tsai, Y.-C. Chen, B.-L. Lin, and C.-K. Sun, "Studies of $\chi^{(2)}/\chi^{(3)}$ tensors in submicron-scaled bio-tissues by polarization harmonics optical microscopy," *Biophys. J.* **86**(6), 3914–3922 (2004).
25. F. Ganikhanov, S. Carrasco, X. Sunney Xie, M. Katz, W. Seitz, and D. Kopf, "Broadly tunable dual-wavelength light source for coherent anti-Stokes Raman scattering microscopy," *Opt. Lett.* **31**(9), 1292–1294 (2006).
26. M. D. Abramoff, P. J. Magelhaes, and S. J. Ram, "Image Processing with ImageJ," *Biophotonics Int.* **11**(7), 36–42 (2004).
27. G. Okano, H. Matsuzaka, and T. Shimojo, "A comparative study of the lipid composition of white, intermediate, red and heart muscle in rats," *Biochim. Biophys. Acta* **619**(1), 167–175 (1980).
28. C. Hidalgo, "Lipid phase of transverse tubule membranes from skeletal muscle. An electron paramagnetic resonance study," *Biophys. J.* **47**(6), 757–764 (1985).
29. K. I. Popov, A. F. Pegoraro, A. Stolow, and L. Ramunno, "Image formation in CARS microscopy: effect of the Gouy phase shift," *Opt. Express* **19**(7), 5902–5911 (2011).
30. M. D. Levenson, C. Flytzanis, and N. Bloembergen, "Interference of resonant and nonresonant three-wave mixing in diamond," *Phys. Rev. B* **6**(10), 3962–3965 (1972).
31. H. M. Warrick and J. A. Spudich, "Myosin structure and function in cell motility," *Annu. Rev. Cell Biol.* **3**(1), 379–421 (1987).
32. R. Dominguez and K. C. Holmes, "Actin structure and function," *Ann. Rev. Biophys.* **40**, 169–186 (2011).

1. Introduction

Muscle characterization using light microscopy has attracted attention as it provides important insights into problems related to contractile physiology [1,2]. The detailed mechanisms underlying muscle contraction and the role played by the structurally and functionally complex T-tubular system in muscle excitation-contraction coupling as well as myofiber architecture are not well understood. This is highlighted by works of Savio-Galimberti *et al.* [3] examining the structural T-tubular network of rabbit heart muscle and Murphy *et al.* [4] indicating that T-tubular components are involved in muscle fiber architecture.

Novel imaging techniques based on nonlinear optical phenomena have been recently adapted in microscopy of biological specimens and successfully applied to tissue characterization [5–13]. Multiphoton fluorescence microscopy, based on the nonlinear optical excitation of intrinsic or extrinsic fluorophores, is a powerful technique for tissue imaging

with sub-micron spatial resolution [5,6]. However, despite its many advantages, the fluorescence based imaging approach is limited in its applications to media containing natural fluorophores. The method's wider applications rely on tissue or cell labeling with organic or inorganic fluorophores. These, however, may have adverse effects due to toxicity [14,15] and photobleaching [16,17].

Second harmonic generation (SHG) [7,8], third harmonic generation (THG) [9,10] and coherent anti-Stokes Raman scattering (CARS) [11–13] are among the key techniques that provide label free imaging of biological media. Since those techniques do not require labeling and do not involve electronic population transfer, toxicity and photo-bleaching effects are nonexistent. The nature of the nonlinear optical effects based on detection of material properties tied to second- (i.e. SHG) or third-order nonlinear susceptibility (i.e. THG, CARS) allows the gathering of different but highly complementary information about the molecular and supramolecular architecture of tissues [13].

The SHG effect is strong in noncentrosymmetric media and has been successfully applied in microscopy applications studying the nonlinear optical response of labeled cell membranes [7], collagen-type-I structures [8], microtubules [18] as well as myosin of the skeletal muscle [19]. CARS microscopy was demonstrated first by Duncan *et al.* in 1982 [20]. Zumbush *et al.* [21] showed the feasibility of CARS microscopy for probing sub-femtoliter volumes within biological cells. Recently, CARS microscopy has been successfully implemented to image cellular outlines within live mouse tissue [11], peripheral axonal myelin [12], the collagen sheets of fascia [13], and lipid storage in living organisms [22].

As was mentioned above, SHG can only be observed in tissue structures that possess a noncentrosymmetric biomolecular organization and is thus limited to very specific biological structures. Ralston *et al.* [23] used a combination of two-photon fluorescence and SHG microscopy to study non-contractile inclusions and sarcomeric anomalies in skeletal muscle. These types of data represent a good example of a structure where SHG microscopy does not provide sufficient information. Chu *et al.* [24] have used a combination of SHG and THG microscopies to image skeletal muscle. The THG signal from skeletal muscle was found to be very weak and was only observed within the actin bands. CARS microscopy is also based on a third-order nonlinear susceptibility ($\chi^{(3)}$) response, but the generated signal is much more intense compared to THG due to the fact that the phase matching condition is almost perfectly met in the forward direction. In addition, CARS offers chemical sensitivity through the imaginary component of $\chi^{(3)}$ wherever a vibrational Raman active resonance is present.

The goal of our studies was to probe and identify the main components of a sarcomere unit of skeletal muscle using nonlinear optical techniques relying on intrinsic second- and third-order nonlinearity responses of the muscle tissue. We were able to detect the entire functional sarcomere unit including the conducting T-tubular system and individual myofibrils that are not easily identified by standard light microscopy techniques. Using CARS microscopy we were able to visualize subsarcolemmal organelles such as mitochondria and cell nuclei, including their substructures.

2. Experimental section

2.1. Sample preparation

Age matched (6 weeks old, male) adult C57/B6 mice were sacrificed (Charles River Laboratories International Inc., MA, USA). Their hind legs were harvested and the triceps surae muscles excised and fixed in 4% paraformaldehyde or 10% formalin. After max. 4-6h of fixation individual muscle fibers as well as fiber bundles were isolated from the triceps surae muscle using a dissecting microscope. After incubating and washing the excised muscle block in collagenase-PBS (Sigma®) solution and 1xPBS solution, the muscle fibers were transferred onto 100 μ m thick coverslips (VWR International, West Chester, USA; 24mmX60mm, No.1) treated with 3-aminopropyltriethoxysilane (APES) or gelatin-chromium potassium sulfate

solution (Gelatin type A- Sigma®, Chromium potassium sulfate, Sigma) for better tissue adhesion. Individual muscle fibers and muscle fiber bundles were kept in 1x PBS solution and washed with 0.01% TritonX-100 -PBS solution to remove lipid remnants that are not part of the structural muscle fibers. Some of the fiber bundles used for the experiments were in the rigor state fixed by formaldehyde fixation.

2.2. Picosecond laser sources for CARS and SHG and scanning microscope

The CARS process can be enabled using two high peak power laser pulses at different wavelengths that are called 'pump' and 'Stokes' pulses. In order to obtain CARS images targeting certain molecular vibrations, the 'pump' and 'Stokes' beam wavelengths have to be tuned so that their optical frequency difference matches the molecular vibration frequency. The CARS signal is detected at the anti-Stokes wavelength that is blue shifted with respect to the 'pump' by the vibration frequency value.

The laser system that was used to generate CARS and SHG images consists of a passively mode-locked Nd:YVO₄ laser (High-Q Laser GmbH) operating at 1064.2 nm (7 ps, 10W, 76 MHz). Most of the output power of the Nd:YVO₄ is used to synchronously pump an optical parametric oscillator OPO (Levante, APE-Berlin) with intracavity-doubling of the signal wave. The OPO output is tunable (~801-822 nm) and delivers 5 ps pulses at a 76 MHz repetition rate with average power of up to 1.5W. We would like to note that this is an OPO system pumped by a 1064 nm picosecond laser. The system was developed by APE-Berlin prior to the most recent model (Emerald) that is pumped by 532 nm ps pulse train [25] and which provides a much wider tuning range for the 'Stokes' pulses. The output was used as the 'pump' beam while a smaller fraction of power from the Nd:YVO₄ laser was used as a source of 'Stokes' photons in the CARS process. Achromatic half-wave plates were introduced into both optical arms. The laser beams are collinearly combined with a 950 nm long pass dichroic mirror and the temporal overlap between the 'pump' and the 'Stokes' was controlled using an optical delay line.

Polarizations of the 'pump' and the 'Stokes' beams were set using an anti-reflection coated Glan-Thompson calcite polarizer (Newport model 10GT04AR.16) located before the microscope laser scanner. The average power of each laser beam incident on the image plane was kept at less than 75 mW to prevent the sample from photo-damage. We verified that the resulting laser polarization at the back aperture of the microscope objective (Olympus UPLSAPO 60XW, NA = 1.2) was linear while the laser beam scanner was engaged.

SHG images were obtained using picosecond pulses provided by the OPO output at around 816 nm (i.e. the 'pump' beam source used for CARS) in order to achieve perfect pixel-by-pixel overlap with the CARS images. In order to detect SHG images, we used a 30 nm wide bandpass filter with 415 nm center wavelength available from Chroma Technologies, Inc. The CARS signal was detected in the forward direction using a 40 nm wide bandpass filter centered at 660 nm in conjunction with a 750 nm short pass filter to ensure the absence of background signal at high photomultiplier (PMT) detector gain. The laser scanning microscope is an inverted Axiovert 200M microscope with LSM510 scanning module (Carl Zeiss MicroImaging, Inc., Thornwood, USA). The resulting images were analyzed using Image-J software [26].

3. Results and discussion

3.1. Detecting muscle cells, organelles and T-tubular system by CARS microscopy

Figure 1 represents CARS images of striated skeletal muscle fiber where the symmetric stretch Raman active vibration of the CH₂ group was targeted at 2845cm⁻¹. The figure also shows representative examples of areas of fixed *in situ* skeletal muscle with additional tissue structures that contain organelles and substructures of various CH₂ concentrations.

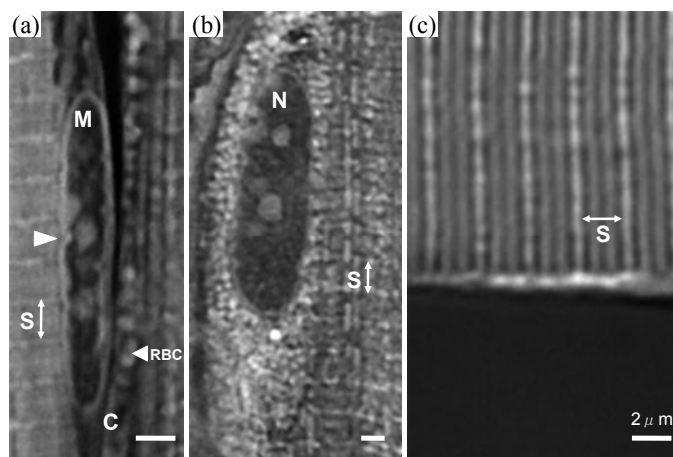


Fig. 1. CARS images of different areas of intact skeletal muscle. The laser frequencies were tuned to target the CH_2 group vibration frequency at 2845 cm^{-1} . The size bar in each subfigure represents $2 \mu\text{m}$. a) Mitochondrion (M) within the striated muscle membrane (sarcolemma) that was identified based on size, shape and clearly discernible cristae outlines. Capillaries (C) between 2 muscle fibers filled with red blood cells (RBC). The image size is $8.9 \mu\text{m} \times 22.9 \mu\text{m}$. b) Image of a nucleus (N) that was identified based on its size, shape and location within the muscle cell. The image size is $20.1 \mu\text{m} \times 38.6 \mu\text{m}$. c) Representative image of a characteristic striated pattern which is similar to the striated pattern seen with conventional light microscopy. The space between two high contrast bands is $\sim 2.6 \mu\text{m}$ which corresponds to the length of a sarcomere. The image size is $15 \mu\text{m} \times 22.5 \mu\text{m}$. The laser beams' polarizations were perpendicular to the muscle fiber axis. The fiber axis on parts (a) and (b) is along the vertical direction of the figure whereas for part (c) it is along the horizontal direction.

Figure 1 (a) shows an area of adjacent skeletal muscle fibers in rigor with several contracted sarcomeres (S) and a capillary filled with red blood cells (RBC). We can identify skeletal muscle organelles, such as mitochondria (M) and sarcolemma substructures. The mitochondrion can be quite clearly identified by its prominent localization in the subsarcolemmal region and its defining substructures. In particular, we can observe a thick mitochondrial membrane and numerous cristae outlines indicated by the triangle symbols on Fig. 1a. The mitochondrion has a characteristic elongated shape with a size of $2\mu\text{m} \times 16\mu\text{m}$. In many tissues, and in skeletal muscle in particular, the number and size of mitochondria vary strongly ($1\text{-}25 \mu\text{m}$) depending on the type of skeletal muscle. Red muscle with predominant type-I fibers, have a higher lipid content. In contrast, white muscle, with predominantly type-II fibers has reduced lipid content [27]. Figure 1 (b) shows a much-increased level of high contrast granulations within the muscle cell compared to Fig. 1 (a) indicating a higher concentration of CH_2 dense molecules, such as lipids. This observation strongly suggests that we deal with red muscle containing more of type-I fibers. Figure 1 (b) clearly shows a muscle cell nucleus given its size ($\sim 6.5\mu\text{m} \times 21\mu\text{m}$), elongated oval shape and subsarcolemmal localization. Both, the mitochondrion and the nucleus are oriented along the fiber axis. The available sensitivity of the CARS setup allows detection of molecular aggregates and their distribution within the nucleus and mitochondria via their CH_2 group stretch vibrations. These molecular aggregates are of different size and distribution within either organelle in Fig. 1(a) and Fig. 1(b) and show different levels of CARS signal intensity. Figure 1(c) shows the striated pattern of several muscle cell sarcomeres, with the typical banding pattern also observed with conventional light microscopy and using common histological stains. The characteristic distance that reflects muscle structure spatial periodicity (i.e. sarcomere unit length) is found to be around $2.6 \mu\text{m}$. Also, it is clear from the images that the various bands show different contrast strengths. These can be grouped into bands with similar contrast. This strongly indicates that the bands within each of these groups are structurally and

compositionally similar. The highest contrast bands emanate from the sarcolemma, perpendicular to the muscle fiber axis, but parallel to the sarcomere plane. These bands appear to be part of the sarcolemma, and strongly suggest that CARS is able to reveal the T-tubular system. In the discussion the structure is labeled as Z-T in order to indicate the spatial overlap of T-tubules with sarcomere Z-lines.

3.2. Identifying skeletal muscle sarcomere sub-units

Figure 2 shows the SHG (a) and CARS (b) images of the same muscle area that can be compared and analyzed. As expected, Fig. 2(a) demonstrates a characteristic banding pattern. The muscle myosin lacks center of symmetry (noncentrosymmetric) and therefore is a source of strong SHG signal as has been demonstrated in Ref. [19]. The high SHG signal lines correspond to the so-called A-bands. In order to perform the data analysis we followed the signals changes along the cross-sectional lines across the image center. The data are presented in Figs. 2 (c) and (d), respectively. As can be seen in Fig. 2 (c) the noticeably strong signal in the center of the myosin band represents the tail region of the myosin macromolecules. The strong signal results from myosin tails that are densely packed in an orderly fashion such that they give rise to strong second order nonlinearity. In contrast, the myosin heads due to a more globular structure cannot be packaged to the same degree of order thus causing the signal to drop away from the sarcomere center.

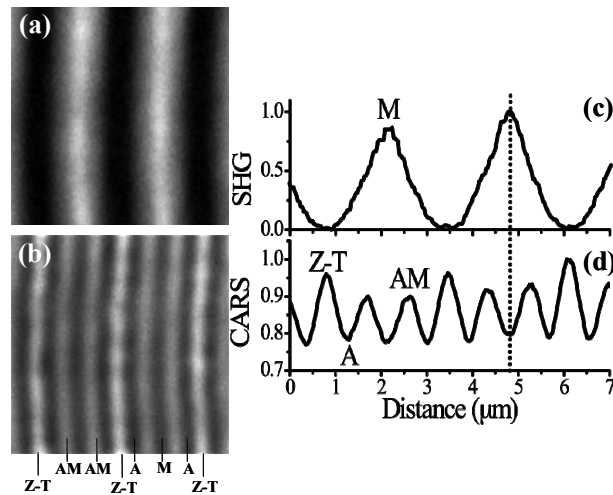


Fig. 2. Images of the skeletal muscle combining SHG (a) and CARS (b) microscopy data. The laser frequencies were tuned to target the CH_2 group vibration frequency at 2845 cm^{-1} . The image area is $7.1 \mu\text{m} \times 7.1 \mu\text{m}$. The SHG (c) and CARS (d) signal profiles along muscle axis showing the corresponding substructures. Nomenclature for the abbreviations is the following: Z-T indicates T-tubules overlapping with Z-lines, A-actin, AM-acto-myosin, M-myosin.

CARS and SHG imaging techniques have been shown to provide complementary data [13] for tissue imaging. The images can be taken simultaneously as the experimental conditions for both techniques are identical, and therefore a precise overlap of the imaging area is feasible. Thus, overlapping the spatially modulated pattern across the CARS and SHG images allows us to precisely identify which band corresponds to which sarcomeric structure. The structures are appropriately labeled in Figs. 2 (c) and 2(d). As was mentioned above, the center portion of the SHG signal corresponds to the compacted tail region of the myosin macromolecules labeled as M-band in the CARS image. This part corresponds to the H-band in conventional histological samples. The head portion of the myosin molecules overlaps with the distal half of the actin molecules while these emanate from the Z-line regions of the sarcomere. Actin bundles do not generate a detectable second harmonic signal [19] Fig. 2 (a). The actin myosin

overlap region in Fig. 2 (b) can be identified as bands of enhanced contrast that are also labeled as AM (acto-myosin) in a CARS image shown in Fig. 3 (b). The increase of the CARS signal for the AM bands is due to the increased protein concentration as actin and myosin are cross-linked in that region via myosin heads. The actin band is labeled as A in Fig. 2(b). In conventional skeletal muscle histology it is labeled as the I band, and includes the Z-line. Signal maxima in the CARS images (see Figs. 2 (b), (d) and Figs. 3(a), and (b)), labeled as Z-T, correspond to signal minima in the SHG image (see Figs. 2 (a), (c)). The Z-T peaks appear to define the sarcomere boundaries and fall within the Z-disc region of conventionally stained skeletal muscle tissue.

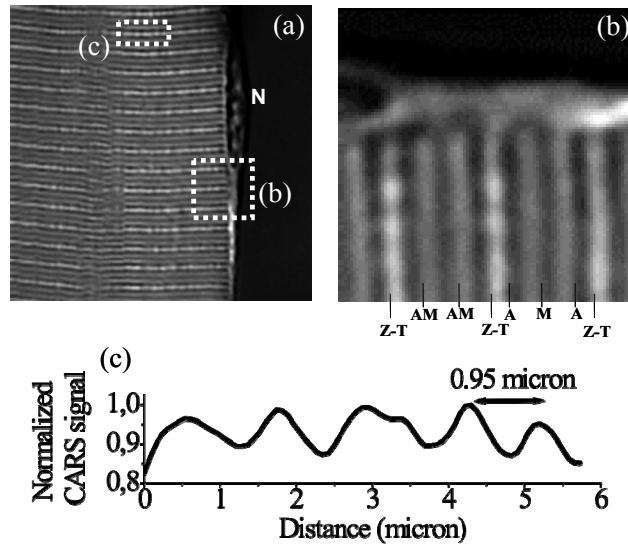


Fig. 3. (a) CARS image of a larger skeletal muscle area ($38.5 \mu\text{m} \times 38.5 \mu\text{m}$), (b) expanded view of the sarcomere structures. Z-line region overlapping with T-tubules, actin band, actomyosin overlap region, and myosin band can be well identified. The corresponding image area (b) is $\sim 7.5 \mu\text{m} \times 7.5 \mu\text{m}$ and rotated counterclockwise by 90° with respect to image (a). (c) The cross-sectional signal data demonstrate periodic CARS signal modulation along Z-T line. This clearly indicates that a single myofibril is resolved in our experiment. The cross-sectional line is drawn along the selected Z-T line that is located within the dashed rectangle on part (a) of the figure.

3.3. Resolving individual myofibril within skeletal muscle

Further examination of the resonant CARS image (Figs. 3 (a, b)) shows the high contrast signal of the muscle cell membrane that contains, in its subsarcolemmal space, what appears to be an elongated myofiber nucleus. It is evident from images on Figs. 3 (a) and (b) that the highest contrast band that is labeled as Z-T emanates from the sarcolemma. The band is aligned perpendicular to the muscle fiber axis thus being parallel to the sarcomere plane. Excellent spatial resolution provided by CARS along with its ability to highlight resonant structures allowed us to reliably detect the fibrillar elements of the muscle fiber. In other words, using CARS we were able to highlight individual muscle fibrils (e.g. myofibrils, actin fibrils). This important feature has not been detected in any previous in situ muscle or T-tubule imaging experiments [19,23].

Figure 3(c) clearly demonstrates the capability to detect the key fiber contractile building blocks. Indeed, one can see that the CARS signal is spatially modulated along the T-tubule axis as well as along the other sarcomere bands where the modulation is less pronounced. The spatial modulation length is approximately $\sim 1\mu\text{m}$ which corresponds to a characteristic myofibril diameter. Thus, we were able to visualize the entire skeletal muscle structural

elements from myofibrils to its organelles including T-tubular network. We believe that we can clearly resolve individual myofibril due to the following reasons. (i) We are able to detect both SHG and CARS signals with high signal-to-noise ratios. In fact, a closer look reveals the spatial signal modulation due to myofibrils. This can be observed in the SHG images as well though the modulation is very weak. (ii) The reasons that myofibrils are highlighted well in the CARS images are due to two key factors. First, as it follows from image in Fig. 3 (b), the t-tubular membranes rich in phospholipids [28] are located within the Z-T bands. The t-tubules are located in the outer-shell of the myofibril. Therefore, as the pump and Stokes laser beams are scanned across the myofibril, the spatial distribution of phospholipids and the resulting number of CH₂ bands within the focal volume is varying and the resulting CARS signal gets modulated. This has a similarity with observations and discussions presented in a recent publication by Popov *et al.* where authors investigate the effect of the Gouy phase shift on image formation and signal strength in CARS microscopy [29]. Second, CARS microscopy compared to SHG can deliver better spatial resolution (20% better in lateral dimension) given the fact that the signal depends on a power density product of the three waves as opposed to just two in the case of SHG. Thus, the spatial distribution of the phospholipids within the Z-T bands and the higher spatial resolution of CARS turned out to be the key points that allowed to detect individual myofibrils.

3.4. Spectroscopic contrast ratios across skeletal muscle sarcomere

Thus far we have focused on structural information that can be obtained utilizing simultaneous SHG and CARS imaging modalities. In particular, we have been able to visualize and identify the T-tubular network (Z-T region) that emanates from sarcolemma. T-tubules as invaginations of the sarcolemma contain high concentration of phospholipids [28]. In order to confirm that T-tubules are within the Z-T band we compared CARS microscopy data taken for Raman shift frequencies that are close and away from the symmetric stretch CH₂ vibration line that is characteristic for lipids. Thus, by comparing the degree of spectroscopic contrast within CARS images we can determine that the T-tubules are in fact within the detected Z-T band. The measurement also provides information about the relative concentration of submolecular units that contain CH₂ groups. For this purpose, CARS images of the mouse skeletal muscle are taken at Raman shifts of $\Delta\omega = 2845 \text{ cm}^{-1}$ (Fig. 4(a)) and $\Delta\omega = 2970 \text{ cm}^{-1}$ (Fig. 4(b)).

The top part of both images in Figs. 4(a, b) represents the skeletal muscle area whereas the bottom represents the signal from the buffer solution in which the muscle fibers were placed. The CARS buffer signal, arising from the four-wave mixing process in water and involving 'pump' and the 'Stokes' laser pulses, is non-resonant and, therefore, it can serve as a reference signal for CARS data normalization. The polarizations of both 'pump' and 'Stokes' fields are perpendicular to the fibrillar axis (i.e. they are parallel to the Z-line region). As can be seen from the figures, the CARS signal is stronger at $\Delta\omega = 2845 \text{ cm}^{-1}$ compared to $\Delta\omega = 2970 \text{ cm}^{-1}$ across all imaged bands of the muscle sample. This can also be observed in quantitative terms in the CARS spectrum data presented in Fig. 4(c). It should be noted that beyond $\Delta\omega = 3000 \text{ cm}^{-1}$, the CARS spectrum might be contaminated by contributions from multiple Raman active vibrations of water. However, the contribution is still fairly weak at that Raman shift to considerably alter the shape of the spectrum shown on Fig. 4(c). The typical periodic structures of the skeletal muscle are clearly resolved again in both cases. The much higher signal observed at $\Delta\omega = 2845 \text{ cm}^{-1}$ is due to the high concentration of molecular structures that are rich in CH₂ groups. As was expected, our data confirm that the Z-T band is at higher lipid concentration based on the quantitative data presented in Fig. 4(d). Indeed, the resonant CARS signal enhancement ratio (i.e. $S_{\text{CARS}}(\Delta\omega = 2845 \text{ cm}^{-1})/S_{\text{CARS}}(\Delta\omega = 2970 \text{ cm}^{-1})$) for the Z-T band is ~2.85 versus ~2.55 for the other sub-structures within the sarcomere. The CARS signal from the muscle area in Fig. 4(b) is smaller compared to the one generated within the buffer solution. This is due to the dispersive nature of the real and imaginary components of

the third order nonlinearity ($\chi_{\text{vib}}^{(3)}$) near the vibrational resonance. Thus, the destructive interference of the two parts attenuates the total intensity at the anti-Stokes frequency [30].

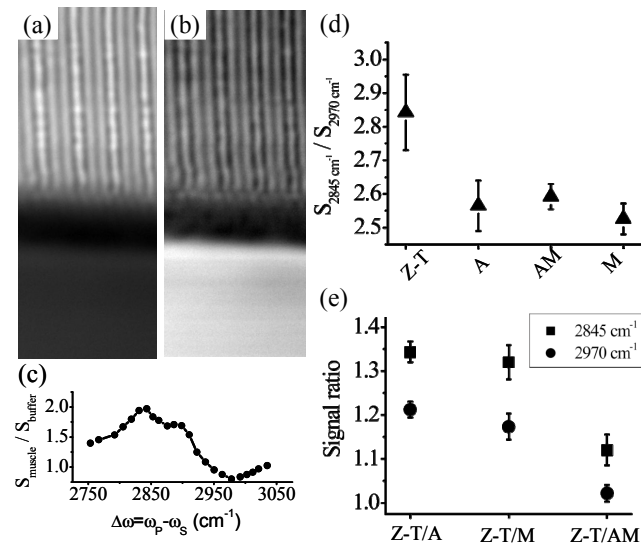


Fig. 4. CARS images obtained for targeted Raman shift frequencies of 2845 cm^{-1} (a) and 2970 cm^{-1} (b). The image size is $10.8 \mu\text{m} \times 27 \mu\text{m}$. The bottom part of the images represents the area that is occupied by the buffer solution. The PMT detector gain and the laser beam intensities were increased for the image obtained at $\Delta\omega = 2970 \text{ cm}^{-1}$ to better highlight the part that outlines the sarcomere structure. Part (c) represents the averaged (over multiple bands) CARS spectrum of the muscle area. The resonant CARS signal enhancement ratios (i.e. $S_{\text{CARS}}(\Delta\omega = 2845 \text{ cm}^{-1})/S_{\text{CARS}}(\Delta\omega = 2970 \text{ cm}^{-1})$) for each sarcomere sub-structure are quantified in part (d). The corresponding signal ratios at the two different vibration frequencies are shown in part (e). The laser beams' polarization condition is the same as for the data presented in Fig. 1 (c).

By carefully examining Figs. 4(a) and 4 (b), we observe qualitatively that the signal in the Z-T band is higher compared to the signal of the other sarcomere components, i.e. actin, actomyosin and myosin. This qualitative observation is summarized in Fig. 4 (e). The signal ratios in Fig. 4(e) were obtained by averaging throughout the image and are presented for the Z-T band with respect to the actin (A), actomyosin (AM) and myosin (M) sub-structures. In other words, those signal ratios are obtained for a large number of sarcomeres by determining the ratios of the Z-T line peaks to the peaks of A, AM and M. All signal ratios are higher at $\Delta\omega = 2845 \text{ cm}^{-1}$ compared to the values at $\Delta\omega = 2970 \text{ cm}^{-1}$, indicating that the CARS signal decreases more in the Z-T bands than in the other sub-structures of the sarcomere when the targeted Raman shift is changed to higher frequency.

3.5. Polarization dependent CARS response of skeletal muscle sarcomere sub-units

Up to now, we have discussed data that were obtained with laser polarizations set perpendicular to the muscle fiber axis. In this study we also addressed the response of the muscle structure to a change in laser beam polarization conditions. The expectation is that, due to the α -helical protein structure within the different sarcomere bands one should observe a difference in CARS signal from the sub-structures as the angle between the laser polarizations and the α -helix axis is changed. It is known that the α -helical chains representing the myosin and actin bands have their main axis aligned along the muscle fiber axis. Thus, it would be useful to obtain data that correspond to at least two cases, (i) when the laser polarizations are parallel and (ii) perpendicular to the muscle fiber axis. Figures 5 (a), (b) represent CARS images obtained at the vibrational resonance frequency of 2845 cm^{-1} .

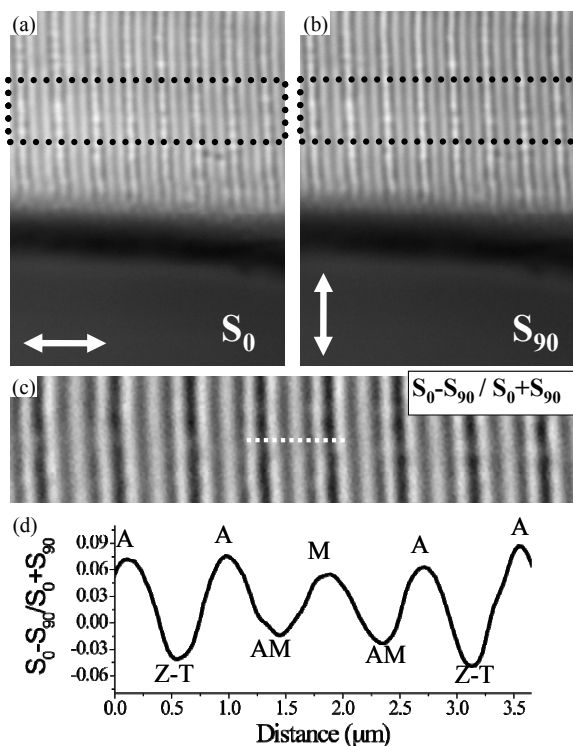


Fig. 5. CARS data for the striated skeletal muscle that show a different response of sarcomere components to different laser electric field polarization thus highlighting their alignment with respect to the muscle fiber axis. CARS images were obtained for the muscle fiber area interfacing with buffer solution. Both images on (a) and (b) have been acquired when the targeted Raman shift frequency was 2845 cm^{-1} . For the image on part (a), the laser polarization for both beams were parallel to each other and also parallel to the fibrillar muscle axis (thus being perpendicular to the Z-T lines). For the image on part (b), the laser polarizations were again parallel to each other but perpendicular to the fibrillar muscle axis (thus being parallel to ZT-lines). Part (c) of the figure represents post-processed data (differential signal) that was derived from the two images above. Namely, CARS signal that corresponds to the data on part (b) was subtracted from the CARS signal on part (a) and normalized to the sum of both signals. Part (d) of the figure represents the differential signal change along the cross-sectional dashed line drawn throughout the center of the image on part (c).

In Fig. 5(a), laser polarizations were set parallel to the muscle fiber axis, whereas Fig. 5 (b) represents the perpendicular case. Qualitative comparison of the images reveals noticeable differences. The differences can be much better highlighted for the differential signal data. In particular, the image represented in Fig. 5 (c) was derived from the original images shown in (a) and (b) using the following expression for the data processing: $\frac{S_0 - S_{90}}{S_0 + S_{90}}$, where

S_0 corresponds to the CARS signal in Fig. 5(a) while S_{90} corresponds to the same in part (b). Also, from Fig. 5(c), we can observe that the sarcomere length can be measured with a better precision. The measured length of $\sim 2.6\mu\text{m}$ matches well what was determined using the data of Fig. 1(c). In Fig. 5(d), we present the differential signal change along the cross-sectional dashed line drawn throughout the center of Fig. 5(c). Three distinct conclusions can be drawn from this figure. First, the CARS signals in the actin and myosin regions are larger when the laser polarizations are parallel to the muscle fiber axis. Second, the CARS signal from the Z-T line region is larger when the laser polarization is perpendicular to the fiber axis. Third, the

differential signal is close to zero in the acto-myosin region. As mentioned above, the actin and myosin bands are composed of protein chains with their main axis parallel to the muscle fiber axis while in the Z-T line region the protein chains are perpendicular to the axis and in the plane of the Z disk. Our observations suggest that the preferential alignment of the molecular axis is along the fiber axis thus giving rise to a higher CARS signal. Using a similar argument, the absence of a CARS signal change within the acto-myosin region for the two distinct polarization cases can be explained by the following: in the AM bands there are myosin heads that are almost perpendicular to the myosin tails which are in turn parallel to the muscle fiber axis. Those heads are responsible for the cross-linkage of myosin to actin proteins. Based on crystallographic studies [31,32], we can speculate that the polarization dependence observed in Fig. 5 is rather due to the electronic contribution of $\chi^{(3)}$ as the CH_2 groups within the myosin and actin proteins are not preferentially aligned along any directions. Our measurements show that CARS microscopy has the ability to measure the overall organization of the sub-micron sarcomeric sub-structures of the skeletal muscle.

4. Conclusion

We report on simultaneous application of SHG and CARS microscopy that allowed us to identify functional contractile sub-units of the skeletal muscle. Using CARS microscopy we were able to visualize muscle fiber organelles such as mitochondria and cell nuclei, including their substructures. Other techniques require specific staining in order to visualize and identify the same. Based on our data we were able to distinguish between red and white muscle fiber (or type-I and type-II) types. The superior spatial resolution and high sensitivity of CARS microscopy allowed us to resolve individual myofibrils within the sarcomere. Also, we have demonstrated the detection of the muscle cell membrane highlighted by its lipid content. Structures that emanate from sarcolemma are identified as T-tubules through the specific spectroscopic capability of CARS microscopy. We observed noticeable changes in spectral response coming from T-tubules due to their higher lipid concentration. Structures within the sarcomere respond differently to laser polarization change. In particular, we confirmed that the two key proteins (actin and myosin) that are responsible for muscle contraction display a molecular organization consistent with their alignment along the muscle fiber axis.

Acknowledgments

F. Ganikhanov thanks West Virginia Nano, NSF-CAREER (DBI-0952532), and NSF-ECCS (EPDT-0925437) for financial support. Authors thank Joe Rowley of WVU for his help. B. R. Olsen acknowledges support from National Institutes of Health grant AR36819. F. Légaré acknowledges the support of the Canada Foundation for Innovation, the Canadian Institute for Photonic Innovations, The Natural Sciences and Engineering Research Council of Canada, and the Fonds Québécois de la Recherche sur la Nature et les Technologies.